Remote Sensing of Environment 124 (2012) 653–665

Contents lists available at SciVerse ScienceDirect

Remote Sensing of Environment

journal homepage: www.elsevier.com/locate/rse

Multi-sensor derivation of regional vegetation fractional cover in Africa

K. Guan *, E.F. Wood, K.K. Caylor

Department of Civil and Environmental Engineering, Princeton University, Princeton, NJ, 08544, USA

A R T I C L E I N F O

Article history:
Received 20 June 2011
Received in revised form 27 May 2012
Accepted 3 June 2012
Available online 17 July 2012

Keywords:
Vegetation fraction
Africa
NDVI
Backscatter coefficient
Vegetation optical depth
AVHRR
QuickSCAT
AMSR-E
TRMM

A B S T R A C T

A spatially continuous field of landscape fractional covers of tree, grass and bare soil is required at regional and continental scales for earth system modeling and environmental monitoring. Climate and its variability drive vegetation fractional cover over time and space. For savanna ecosystems, precipitation plays the main role in shaping vegetation composition. In this study, we estimate land cover fraction at a satellite pixel scale by employing an existing 'Mean-Sensitivity Unmixing Algorithm' (MSUA), which is based on a state space defined by two key variables: (1) mean pixel values (referring to mean vegetation states), and (2) inter-annual sensitivity of pixel values to precipitation (referring to vegetation sensitivity to precipitation). We define these two variables through a multi-sensor assessment of three vegetation remote sensing datasets, namely (i) Normalized Difference Vegetation Index (NDVI), based on the visible and near-infrared bands from the Advanced Very High Resolution Radiometer (AVHRR); (ii) backscatter coefficients (dB) from the NASA QuikSCAT active-microwave scatterometer; and (iii) Vegetation Optical Depth (VOD) based on NASA Advanced Microwave Scanning Radiometer on EOS (AMSR-E) passive-microwave radiometry measurements. A merged satellite-gauge precipitation dataset from the Tropical Rainfall Measuring Mission (TRMM) version 3B42V6 is used. The three remote sensing datasets show generally similar but distinctive performances in characterizing the two key variables over various land cover types. NDVI and VOD perform better than dB in characterizing land cover variation based on mean pixel values; while dB represents more reliable and robust vegetation sensitivity to precipitation. By using NDVI for mean vegetation states and dB for inter-annual variability of vegetation to precipitation, we develop an improved fractional cover product. We find that our product agrees well with the tree fraction derived from high-resolution images for natural vegetation regions, and can reproduce the distinctive land cover pattern of grass and bare soil in the Moderate Resolution Imaging Spectroradiometer (MODIS) land cover product. For cropland-mixed regions, our tree fraction is overestimated since human impacts (e.g. irrigation) have not been accounted for in the MSUA. The improved performance from our approach is achieved by the synergistic use of the three vegetation remote sensing datasets, and their physical interpretations have been discussed to support the validity of this approach.

1. Introduction

Vegetation structure and composition play an important role in understanding ecosystem functioning (e.g. fire and grazing), as well as in managing ecosystem services (e.g. deforestation monitoring) (Hirota et al., 2011; K'efi et al., 2007; Mayaux et al., 2005; Miles et al., 2006). Vegetation fractional cover is also crucial for representing sub-pixel heterogeneity in climate and land-surface models (Avissar & Verstraete, 1990; Gutman & Ignatov, 1998; Zeng et al., 2000). Thus a spatially-continuous and reliable representation of vegetation fractional cover is required at regional and continental scales. This is especially true for savanna ecosystems, which are typically characterized as a mixture of woody and herbaceous vegetation (Sankaran et al., 2005; Scholes & Archer, 1997). Savanna ecosystems comprise approximately 20% of the global land area and up to 40% of the African continent (Scholes & Walker, 1993). This vast terrestrial extent makes savanna ecosystems a significant component in the global terrestrial carbon budget (Grace, 2004; Randerson et al., 1997). Possible degradations in savanna ecosystems induced by drought, overgrazing, fire regime shift, and woody encroachment in the context of a changing climate warrant a better quantification of the relative abundance of vegetation fractional covers.

Climate variability shapes the landscape structure at various spatial and temporal scales, with precipitation being the major driving force in characterizing vegetation composition in savanna ecosystems (Good & Caylor, 2011; Rodriguez-Iturbe & Porporato, 2004; Scanlon & Albertson, 2003). Different vegetation types respond differently to precipitation patterns. In particular, herbaceous plants utilize dense and shallow root systems to use ephemerally available water in the upper soil layer, while woody plants have a root system which can penetrate deeper soil layers and access a more stable supply of soil water (Scanlon et al., 2002). In addition, herbaceous plants in dry/semi-dry savanna ecosystem have a photosynthetic pathway (C4) that synthesizes more carbon per unit of water than do C3 woody plants (Ehleringer & Monson, 1993). For these reasons, herbaceous plants are more sensitive to

* Corresponding author. Tel.: +1 609 258 6383.
E-mail address: kguan@princeton.edu (K. Guan).

0034-4257/$ – see front matter © 2012 Elsevier Inc. All rights reserved.
doi:10.1016/j.rse.2012.06.005

precipitation and have a relatively low above-ground biomass. Woody plants, on the other hand, are less sensitive to precipitation variability with a relatively high above-ground biomass (Scanlon et al., 2002; Scholes & Walker, 1993). Thus it is possible to estimate sub-pixel fractional covers by leveraging the differences in trees and grasses in terms of their above-ground biomass and their sensitivity to precipitation.

Remote sensing (RS) provides the most efficient way to derive fractional covers at regional and global scales. At medium to coarse resolutions (>250 m), representative RS-based approaches for deriving vegetation fractions include:

(i) spectral-based supervised classification (hereafter referred as 'SC', e.g. Friedl et al., 2002; Hansen et al., 2003);
(ii) spectral-based linear unmixing techniques ('SU', e.g. DeFries et al., 1999; Okin, 2007);
(iii) relative vegetation abundance approach scaled by maximum and minimum vegetation index ('RA', e.g. Gutman & Ignatov, 1998; Zeng et al., 2000);
(iv) multi-angle geometric-optical model ('GO', e.g. Chopping et al., 2008, 2009); and
(v) 'Mean-Sensitivity Unmixing Algorithm' (MSUA) based on the different responses of land covers to precipitation variability (Scanlon et al., 2002).

The spectral-based approaches (SC and SU) require spectral characterizations of each land cover component, which are usually determined from training datasets and associated empirical knowledge (Friedl et al., 2002). The RA approach constructs a ratio scaled by maximum and minimum vegetation index values, and this approach does not account for the heterogeneity of different plant functional types within each pixel. The GO approach takes the three-dimensional structure of landscape into account by using multi-angle geometric-optical models, and has shown great potential for representing savanna structure (Chopping et al., 2008), but local calibration from high-resolution imagery is usually required. These four methods are either unable to extract sub-pixel fractional covers or require calibration and/or empirical knowledge. The 'Mean-Sensitivity Unmixing Algorithm' developed by Scanlon et al. (2002) provides a different linear unmixing algorithm for sub-pixel fractional cover that does not require calibration or other empirical inputs. The algorithm utilizes the knowledge that different plant functional types have different vegetation responses to precipitation, and constructs a state space formed by two key variables for linearly decomposing sub-pixel fractional covers:

(1) the mean vegetation states;
(2) the inter-annual sensitivity of vegetation to precipitation.

The algorithm objectively determines the endmembers on the basis of an optimal fit to the observed data. Scanlon et al. (2002) applied the MSUA concept to a Kalahari savanna transect with a precipitation gradient of 300–1600 mm/yr using Normalized Difference Vegetation Index (NDVI) as the vegetation dataset. In tropical regions with extensive cloud cover, the MSUA's effectiveness may be limited if it only uses the visible–near infrared (Vis–NIR)-based NDVI.

Vis–NIR RS has the longest history of vegetation monitoring. For example, the Vis–NIR-based vegetation index record from the AVHRR is from 1981 till present (Tucker et al., 2005). But the accuracy of Vis–NIR RS products is affected by a number of factors include incomplete atmospheric corrections (Tanre et al., 1992; Viovy et al., 1992), the inability of the bidirectional reflectance distribution function (BRDF) to represent the surface anisotropy property (Chopping et al., 2002), and cloud cover that prevents Vis–NIR surface measurement especially for tropical regions. Cloud fractions significantly increase during the rainy season in tropical Africa (Fig. 1), which overlaps with the growing season. An analysis of the MODIS reflectance product MOD09 shows that the daily NDVI suppression is correlated with cloud fraction during the growing season in Africa (results not shown here), and similarly for the AVHRR-based product (Tang & Oki, 2007). Maximum-value compositing (MVC) (Holben, 1986; Viovy et al., 1992), temporal/spatial averaging (Zhao et al., 2005), or the stricter cloud-pixel-screening approaches (Heidinger et al., 2002) when applied to Vis–NIR RS datasets can overcome this problem to a certain extent. But cloud residual noise is still hard to separate from the true vegetation signals, and regions with extensive cloudiness often have large gaps (or significant noise) in their product during the growing seasons. The low signal-to-noise ratio in vegetation products causes problems in quantifying intra- and inter-annual sensitivity of vegetation states to climate variability, particularly in these regions. Thus, alternative measurements are required, such as those from microwave sensors that have the ability to penetrate clouds.

In this paper, we apply the MSUA algorithm to derive the vegetation fractional covers over a tropical savanna region with a broad precipitation gradient ranging from 200 to 2000 mm/yr. We utilize and assess the capability of three independent RS products to determine two key variables needed by the MSUA: the mean vegetation states and the vegetation sensitivity to precipitation. The three RS datasets are: (i) NDVI, based on Vis–NIR bands in AVHRR; (ii) backscatter coefficients (dB) from NASA's QuikSCAT active-microwave scatterometer; and (iii) Vegetation Optical Depth (VOD) based on NASA's AMSR-E passive-microwave radiometry measurements. Based on a comprehensive assessment of the multi-sensor vegetation datasets with the TRMM 3B42v6 satellite-gauge merged precipitation product, we find that NDVI is most suitable in characterizing mean vegetation states, while dB provides the most robust estimation of vegetation sensitivity to precipitation. By combining these two products, essentially a synergistic use of optical-microwave sensors, a new approach is proposed for deriving fractional vegetation covers. A physical interpretation for how each product responds to vegetation cover and its sensitivity to precipitation is provided to support the validity of the approach.

2. Materials and methods

2.1. Study area

The study domain (Fig. 1) is approximately 700 km wide and 2,800 km long, running southwest from the Ethiopia-Kenya border (4° N) to the Botswana–South Africa border (24° S), and covers a total area of approximately 2.4 million km^2 (including large parts of Kenya, Tanzania, Malawi, Zambia, Zimbabwe, and Botswana). The mean annual precipitation (MAP) across the domain ranges from 200 to 2000 mm/yr (Fig. 1), resulting in widely varying distributions of grass and tree fractions. The MAP is highest in the central portion, and decreases to the southern and northern parts of the domain. The land cover product from MODIS MCD12Q1 shows a similar gradient with the central portion having more woodland, while the southern portion having more shrubland and grassland, and the northern portion being mainly composed of bare ground and grassland.

2.2. Datasets

Table 1 provides an overview of the datasets used in this study. Normalized Difference Vegetation Index (NDVI) is the most extensively-used RS data for vegetation monitoring (Tucker et al., 2005). NDVI is formulated based on the different absorption of chlorophyll-a and -b in green leaves in the red (~690 nm) and near-infrared (~850 nm) frequency bands (Glenn et al., 2008). This results in a unique vegetation spectral feature distinctive of other land cover types (e.g. soil, water and snow). NDVI is defined as:

$$\mathrm{NDVI} = (\rho_{\mathrm{NIR}} - \rho_{\mathrm{Red}})/(\rho_{\mathrm{NIR}} + \rho_{\mathrm{Red}}) \tag{1}$$

where ρ_{Red} and ρ_{NIR} refer to the reflectance at red and near-infrared frequency, corresponding to AVHRR Band one (0.58–0.68 um) and Band two (0.72–1.0 um) in this study. The Global Inventory Modeling and Mapping Studies (GIMMS) NDVI based on AVHRR measurements is

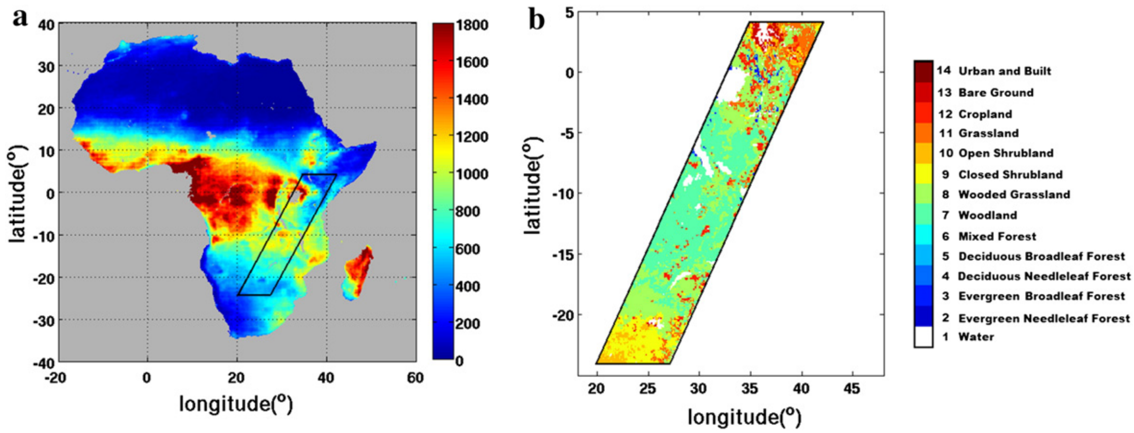

Fig. 1. (a) Mean annual precipitation (MAP) of Africa during years 2000–2010 from TRMM (Regions with MAP above 1800 mm/yr are not distinguished). The study transect is outlined in the black box. (b) Land cover information of the study area from MODIS 1 km land cover product MCD12Q1 (Friedl et al., 2002).

used (Tucker et al., 2005). The time-resolution of the dataset is half-monthly, and the space-resolution is 8 km.

The backscatter coefficients are from the QuikSCAT scatterometer, and it reported in decibels (dB). For convenience, we refer to this dataset as 'dB' hereafter. Scatterometer was originally developed for observing near-surface wind-fields over the ocean (Naderi et al., 1991), and it has also been applied to characterize land surface properties (Frison & Mougin, 1996; Frison et al., 1998; Frolking et al., 2005, 2006; Jarlan et al., 2002; Zine et al., 2005). Because backscatter signals are determined by the roughness and dielectric properties of the surface, they contain information on vegetation properties (in particular the vegetation density/fraction and canopy water content), as well as the soil moisture. Microwave signal frequency and landscape anisotropy also impact the backscatter signals (Magagi & Kerr, 1997). As microwave frequency increases, above-ground photosynthetic biomass of vegetation contributes more to the variation in backscatter dB, and other factors have less impact (McDonald, 1993; Ulaby et al., 1990). This is particularly true for Ku-band scatterometers due to its high frequency (ranging from 12 to 18 GHz), which provides the scientific foundation of using Ku-band dB for vegetation application (Frolking et al., 2005, 2006). The QuikSCAT scatterometer is a Ku-band (13.4 GHz, or 2.1 cm wavelength) instrument with two rotating pencil beam antennas operating in H and V polarizations at an incidence angle of 55° and 46°, respectively, and has two equatorial overpasses per day (0600 and 1800 h). QuikSCAT was launched in 1999 and operated until 23 November 2009 due to the failure of its motor for the spinning antenna. The original spatial resolution of QuikSCAT was 22.5 km, but an enhanced 4.5 km resolution product is used here, which was developed by combining multiple orbit overpasses (Early & Long, 2001; Long et al., 1993). Since H and V polarizations have similar sensitivity to surface characteristics (Hardin & Jackson, 2003), we use H polarization in this analysis.

Vegetation Optical Depth (VOD) is a derived product using a radiative surface emission model based on measured microwave brightness temperatures and other variables as inputs. A number of algorithms for VOD have been proposed (Jones et al., 2009; Njoku & Chan, 2006; Owe et al., 2001; Shi et al., 2008). Here, we use the algorithm of Jones et al. (2009, 2010, 2011). This VOD product is derived at the 25 km spatial resolution using AMSR-E 18.7 GHz frequency daily brightness temperature (Tb) measurement. The algorithm is based on a zero-order $\tau-\omega$ radiative surface emission formulation (Ulaby et al., 1982). At its 25 km resolution, this VOD product explicitly accounts for the effect of open water fraction and land cover information (Jones et al., 2011). AMSR-E is a six-band (6.9 − 89 GHz) dual-polarization radiometer with a rotating dish antenna incidence angle of 55°. Its equatorial crossing times were 0130 and 1330 h, and it ceased operating on 4 October 2011 due to the failure of its antenna motor.

Tropical Rainfall Measurement Mission (TRMM) rescaled multi-satellite rainfall product version 3B42V6 is used as the precipitation dataset. TRMM 3B42V6 is a 3 hourly, 0.25° product based on multi-satellite retrievals that combine microwave and infrared estimates, and are rescaled to match monthly gauge observations using histogram matching (Huffman et al., 2007). The MODIS land cover product MCD12Q1 (Friedl et al., 2002) is used here and is upscaled from 1 km to 10 km based on the dominant land cover types. Our new fractional cover product is validated against high-resolution images from Google Earth Pro (Google, Inc.) in 24 locations with distinctive land-cover fractions during the growing season. Among them, 16 locations are from the Geoeye products and 8 locations are from DigitalGlobe products.

Table 1
Datasets used in this study: the variable fields, resolution and source (product).

Analysis	Data	Temporal resolution	Spatial resolution	Temporal coverage	source
Multi-sensor assessment (half-monthly)	NDVI	Half-monthly	8 km	08/1999–12/2008	AVHRR GIMMS[a]
	dB	4-day	about 4.5 km	08/1999–12/2008	QuikSCAT SIR[b]
	VOD	Daily	0.25°	07/2002–12/2008	AMSR-E(derived)[c]
	precipitation	3 hourly	0.25°	08/1999–12/2008	TRMM 3B42V6[d]
Validation and comparison	Google Earth (Geoeye(16) or DigitalGlobe(8))		Around 4 m	2000–2011	
	VCF	Yearly	500 m	2000–2005	MOD44B[e]
Ancillary data	Land cover		1 km		MCD12Q1[f]

[a] Tucker et al. (2005).
[b] Long et al. (1993), Early and Long (2001).
[c] Jones et al. (2009, 2010, 2011).
[d] Huffman et al. (2007).
[e] Hansen et al. (2003).
[f] Friedl et al. (2002).

Our new product is further compared with another independent vegetation fraction product of MODIS Vegetation Continuous Fields (MOD44B VCF), which provides yearly estimates of the tree fraction based on a supervised regression tree algorithm (Hansen et al., 2003).

2.3. 'Mean-Sensitivity Unmixing Algorithm' (MSUA)

The MSUA follows the work of Scanlon et al. (2002), which is a linear un-mixing model of vegetation fractional covers based on two key fields: (1) mean pixel values, and (2) inter-annual sensitivity of the pixel values to precipitation. The algorithm is applied to the growing seasons as defined in Section 2.4 and assumes minimal large-scale land cover change during the 10 year study period. The algorithm assumes that each pixel is composed of three land cover types (grasses, trees, and bare soil, referred to as 'endmembers'). Each endmember has distinctive characteristics that can be referenced back to the RS products: grass has high sensitivity to precipitation and medium above-ground photosynthetic biomass, trees have lower sensitivity to precipitation and high above-ground photosynthetic biomass, and bare soil has low sensitivity to precipitation and no above-ground photosynthetic biomass. Pixels containing more than one endmember display a mean vegetation state and sensitivity to precipitation, weighted by their respective fractional covers of each endmember. All the pixels are supposed to fall inside a triangle envelope in the 'Mean-Sensitivity Space' (Fig. 2), with three vertices, each associated with one endmember. In turn, each pixel can be decomposed into three fractional covers based on their position inside the space.

In detail, the algorithm is composed of three equations and three unknowns (Fig. 2). The first equation (Eq. 2) requires that the total ground area is composed only of three land cover types: grasses, trees and bare soil, whose fractional covers are three unknowns. This simplification of plant functional types has been found to be an effective representation of savanna ecosystems (Caylor et al., 2006; Scanlon et al., 2002; Scholes et al., 2002):

$$\mathrm{f_g(i) + f_t(i) + f_s(i) = 1} \tag{2}$$

where i refers to a specific pixel inside the transect, and f_x refers to the fraction of endmember x within the pixel i during growing seasons (x = g, t, s, representing grasses, trees and soil respectively).

The second equation (Eq. 3) states that the mean vegetation states during growing seasons in pixel i $(\overline{V_{obs}(i)})$ are equal to the sum of the vegetation states of each endmember, weighted by their corresponding fractional cover, $f_x(i)$:

$$\overline{V_g}f_g(i) + \overline{V_t}f_t(i) + \overline{V_s}f_s(i) = \overline{V_{obs}(i)} \tag{3}$$

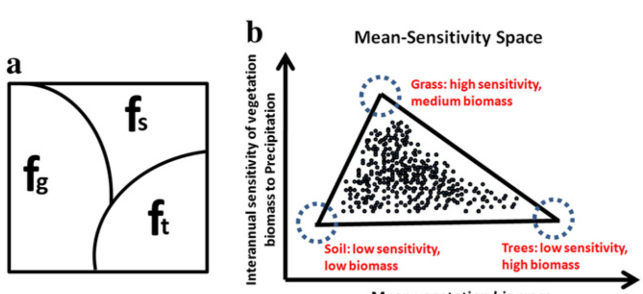

Fig. 2. Schematic diagram of the 'Mean-Sensitivity Unmixing Algorithm' (MSUA) (Scanlon et al., 2002). (a) Each pixel is composed of three land covers: grass (fg), tree (ft) and bare soil (fs). (b) Conceptual 'Mean-Sensitivity Space' of vegetation. Three endmembers are: grass, with high sensitivity to precipitation and medium above-ground photosynthetic biomass; trees, with low sensitivity to precipitation and high above-ground photosynthetic biomass; and bare soil, with low sensitivity to precipitation and low above-ground photosynthetic biomass. Any pixels are supposed to fall inside this space.

where $\overline{V_x}$ represents the mean vegetation states during growing seasons for each endmember inferred from RS data (x = g, t, s). 'Vegetation states' is used here to broadly describe above-ground vegetation characteristics, whose specific meaning for each RS product has been given in detail in Section 4.1.

The third equation (Eq. 4) assumes the overall sensitivity of vegetation to precipitation, $\overline{S_{obs}(i)}$, is also a function of the linearly weighted sensitivities of three endmembers.

$$\overline{S_g}f_g(i) + \overline{S_t}f_t(i) + \overline{S_s}f_s(i) = \overline{S_{obs}(i)} \tag{4}$$

where $\overline{S_{obs}(i)}$ is the inter-annual sensitivity of the pixel value to precipitation, calculated from a linear regression between yearly anomalies of growing-season mean pixel values (dV_{obs} (i)) and yearly anomalies of growing-season total precipitation (dP(i)) over the study period (1999–2008):

$$\overline{S_{obs}(i)} = \left(\overline{\frac{dV_{obs}(i)}{dP(i)}}\right) \tag{5}$$

In Eq. (4), $\overline{S_x}$ refers to the inter-annual vegetation sensitivity to precipitation for an endmember (x = g, t, s).

2.4. Implementation and data processing

Our analysis is conducted at the half-monthly scale, focusing on the most recent decade (1999–2008) due to availability of data (record length: dB-10 years; VOD-7 years; NDVI-10 years). dB and VOD were averaged to half- monthly, in order to smooth the noise and to maintain consistency with the half-monthly NDVI dataset. The datasets were aggregated or interpolated to 10 km for the analysis.

The growing season for each pixel is defined as follows, based on the half- monthly dataset. First, the rainy season is specified as the time period that includes more than 85% of the annual total rainfall. The vegetation growing season is then defined as the rainy season plus a post-season addition that reflects vegetation activity after the end of the rainy season. The addition is calculated to be the length of time until NDVI drops to 10% of its seasonal range (i.e. = NDVImax − NDVImin, where NDVImax is the peak value and NDVImin is the baseline value). Usually the addition length ranges from 0.5 to 2 months, with grassland having shorter lags and woodland longer ones. The above calculation uses mean annual precipitation and mean annual NDVI. Once the growing season is defined, the analyses for three RS data follow the same definition.

In order to find the optimal representation of mean vegetation states and vegetation sensitivity to precipitation, we first compared the corresponding performance of the three RS datasets over different land cover types. After that, the 'Mean-Sensitivity Space' was constructed by identifying pixels with significantly positive regressed sensitivity ($P<0.1$) that would be used to find the endmembers. Then, a 'Simulated Annealing' algorithm (Laarhoven et al., 1988) was used to automatically find the optimal endmembers for the 'Mean-Sensitivity Space', such that the minimum area includes 99% of all the points. Given the endmember values ($\overline{V_t}$, $\overline{S_t}$), ($\overline{V_g}$, $\overline{S_g}$), ($\overline{V_s}$, $\overline{S_s}$), and each pixel's mean $\overline{V_{obs}(i)}$ and sensitivity $\overline{S_{obs}(i)}$, the MSUA (Eq. 2 to Eq. 4) was finally used to get the fractional covers for each pixel in the study domain.

2.5. Validation approach

To validate the quality of the new fractional cover product, we compared our fractional cover with classification results at 24 locations with diverse land cover types spanning the transect (c.f. Fig. 6c) using high-resolution images from Google Earth Pro (Google Inc.). We chose the high-resolution images because they have large spatial coverage and match the scale of our product, unlike field data which is usually collected in plots smaller than 0.1 km^2 (Sankaran et al., 2005) and has a large mismatch in scale with our product. The high-resolution images were chosen based on the following criteria: 1) the overpass time was within the growing season defined in Section 2.4; 2) the scene was cloud-free; and 3) the neighboring landscape was essentially homogeneous. The latter two criteria were visually judged. Each image has the nominal spatial resolution of 4 m, and is approximately 4.4 km^2 in area. The images were then applied to an unsupervised classification algorithm (Iso-Data) in ENVI (Exelis Visual Information Solutions, Inc.) to separate them into 12 classes. We visually merged the classes that overlap with the tree crown area in the classified image. We only extracted the tree fraction from the high-resolution images due to the high accuracy in its identification, while fractions of grass and bare soil were not extracted—since they are still mixed at this spatial level. The detailed results and sample images are provided in the supplementary materials.

We also compare MOD44B VCF with the tree fraction derived from the high-resolution images. The percent tree canopy in MOD44B refers to the amount of skylight obstructed by tree canopies equal to or greater than 5 m in height and is different than the percent crown cover (crown cover = canopy cover + within crown skylight) (Hansen et al., 2003). The latter (percent crown cover) is the definition of tree fraction from high-resolution imagery. Thus, for comparison, we adopt the recommendation of Hansen et al. (2003) to get the crown cover by dividing the MOD44B canopy cover by 0.8.

3. Results

3.1. Multi-sensor assessment of mean vegetation states

Mean growing-season dB and VOD over all years in the study period are compared in Fig. 3 with that of NDVI. Overall, the mean VOD and mean NDVI exhibit a relatively strong linear correlation (Fig. 3b). This also holds in general for correlations within each land cover type based on the MODIS land cover product, as demonstrated by the significant linear correlations between VOD and NDVI, with R^2 ranging from 0.176 to 0.671 for all the land cover types ($P<0.001$, Fig. 3d). NDVI is known to saturated at high values of LAI (Huete et al., 1997), which is not clearly seen from the relationship between NDVI and VOD here. One possible reason is that NDVI does not reach the saturation range, considering relatively low above-ground leaf biomass in this savanna ecosystem. The linear correlation between NDVI and dB (Fig. 3a) is not as high as that between NDVI and VOD (Fig. 3b), and a large scatter in dB is observed across a narrow range of low NDVI values (Fig. 3c). The correlation between NDVI and dB is insignificant for bare ground, and negative for open shrubland. Apart from these two land cover types, other land cover types show significant linear correlations between NDVI and dB ($P<0.001$), with R^2 ranging from 0.162 to 0.581.

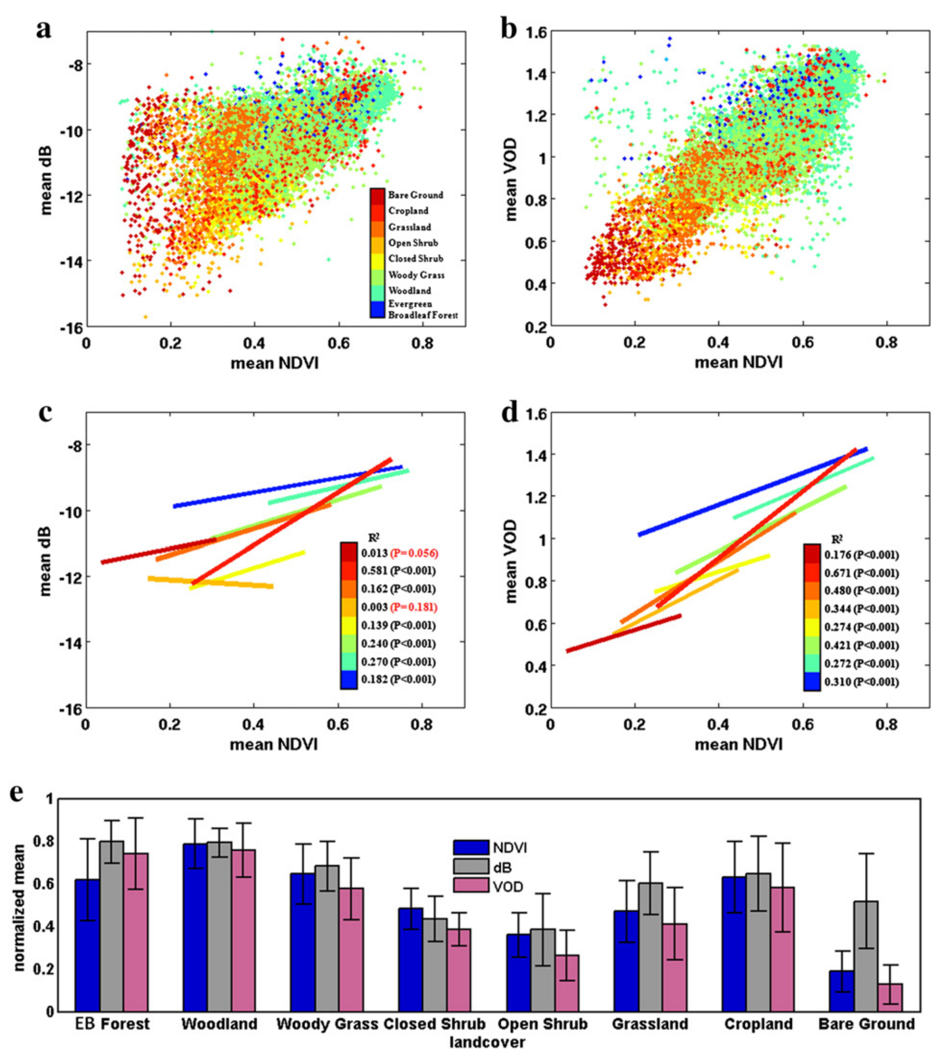

Fig. 3. (a and b) Scatterplots of mean growing-season NDVI–dB, and NDVI–VOD, respectively. Color shading corresponds to land cover types. (c and d) Linear regression slopes for the same land cover types for mean growing-season NDVI–dB, and NDVI–VOD, respectively. (e) Normalized mean value of NDVI, dB and VOD for different land cover types. The normalization is done such that the maximum and minimum values correspond to 1 and 0. 'EB Forest' refers to evergreen broadleaf forest.

The normalized mean values of different land cover types for three datasets are compared in Fig. 3e with error bars showing the standard deviation. As expected, the mean pixel value of bare ground is the lowest, woodland and forest are the highest, and shrubland and grassland are intermediate. Cropland shows a relatively high mean pixel value that is similar to woodland. The major inconsistency is that dB has abnormally high values for bare ground as compared to the two other datasets, probably due to the soil surface roughness effect. This mismatch indicates that dB may fail to represent mean vegetation states when bare soil fraction is a large fraction of a pixel.

3.2. Multi-sensor assessment for inter-annual sensitivity of vegetation to precipitation

The adjusted R^2 of the linear regressions between the annual growing- season NDVI/dB/VOD and precipitation are shown in Fig. 4. Spatial patterns of adjusted R^2 for all pixels, regardless of their significance level, show a similarity across all three RS datasets (Fig. 4 left column), where the northern and some near-equatorial regions have high R^2 (corresponding to relatively low precipitation and shrubland/grassland), and the central region of the domain has low R^2 (corresponding to relatively high precipitation and woodlands). However there are also apparent differences in the three datasets. NDVI has generally lower R^2 than dB and VOD. At the $P<0.1$ significance level, only a small fraction of pixels in the study region show significant correlations (Fig. 4 right column) for NDVI. In the case of dB, the majority of the pixels exhibit significant correlations.

The inter-annual sensitivities of pixel values to precipitation (i.e. the slopes of the linear regression) for the three RS datasets are shown in Fig. 5. All three RS datasets share similar patterns with shrubland having the highest sensitivity to precipitation, and both bare ground and woodland having low sensitivity. But when the percentage of pixels satisfying the significance level ($P<0.1$) is considered, dB is superior to the other two datasets. Except for the case of bare ground, all other land cover types have more than 60% of pixels with significant correlations between dB and precipitation ($P<0.1$), far exceeding the percentages of VOD and NDVI. We further find that many pixels fall in the up-left quadrant in Fig. 5c, which means these pixels exhibit a negative correlation

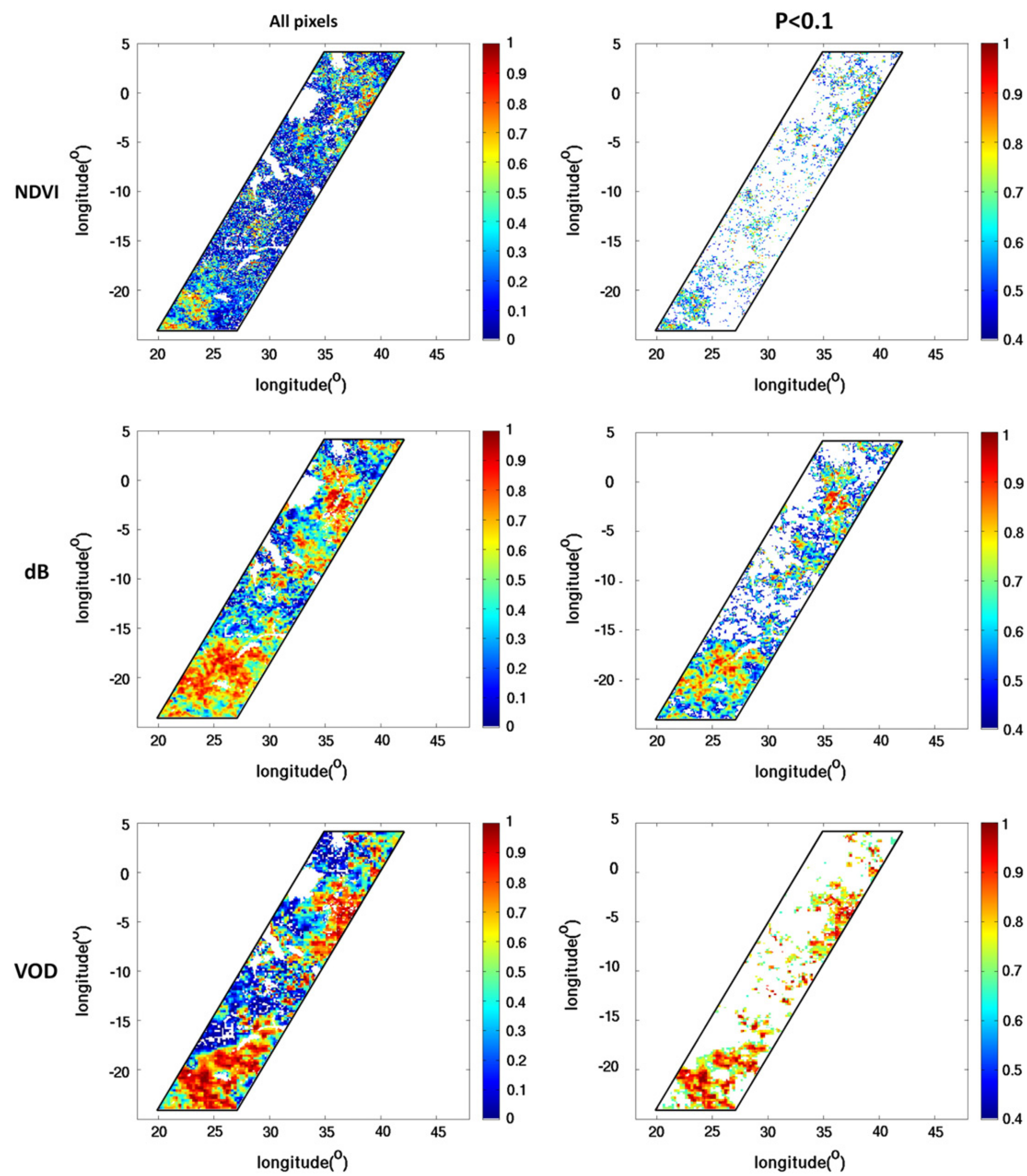

Fig. 4. Adjusted R^2 values for the linear correlation between annual fields of growing season NDVI/dB/VOD and TRMM precipitation. (Left column) all pixels regardless of significance level; (right column) pixels only with significant correlation ($P<0.1$).

between NDVI and precipitation, but a positive correlation between dB and precipitation. The negative correlation between NDVI and precipitation is mostly caused by the cloud contamination for Vis–NIR sensors, but it is largely overcome by the microwave sensors (see detailed discussion in Section 4.1).

3.3. Multi-sensor derivation of fractional covers and its validation

Based on the results of the multi-sensor assessments, we find NDVI and VOD are good in characterizing land cover variations based on mean pixel values, and dB is best to represent vegetation sensitivity. Therefore we merged the use of NDVI (for its higher spatial resolution than VOD) and dB to construct a new 'Mean-Sensitivity Space' for decomposing sub-pixel fractional covers (Fig. 6).

We find our product compares favorably with the tree fraction derived from high-resolution images in locations with natural vegetation ($y = 0.74x + 0.15$, $R^2 = 0.71$, $P = 0.007$, Fig. 7a). However in cropland-mixed locations, our tree fraction is overestimated. The cropland in the study transect is mostly located near water bodies, where irrigation is a popular agricultural management activity. These factors cause the cropland in the transect to have relatively high mean pixel values and low sensitivity to precipitation, which is very similar to trees' response. Since the irrigated cropland is prevalent in the north of Lake Victoria, the derived high tree fraction there is overestimated. This indicates that MSUA is most effective for natural vegetation rather than human-impacted land covers. We find MOD44B VCF generally has lower tree fraction than that derived from high-resolution images ($y = 0.71x - 0.074$, $R^2 = 0.57$, $P = 0.125$, Fig. 7b). Though it is worthwhile to notice that the classification of the high-resolution images may include some short shrubs that are identified as trees due to their similar spectral feature. The MOD44B VCF does not have an overestimation of tree fraction in cropland as found in the MSUA. This is mostly because the VCF algorithm is based on the spectral information, and there is a significant spectral difference between crops and trees. The direct validation of grass and bare soil is difficult due to the lack of field data. But our product has reproduced well the land cover pattern of the MODIS land cover map (Fig. 1b) with the northern part having more bare ground while the southern part having more grass/shrubland.

4. Discussion

4.1. Physical interpretations of the RS datasets

The differences in the three RS datasets are due to their sensitivities to different land surface properties (e.g. vegetation, soil, surface roughness) and atmospheric effects. Understanding the causes of these differences is

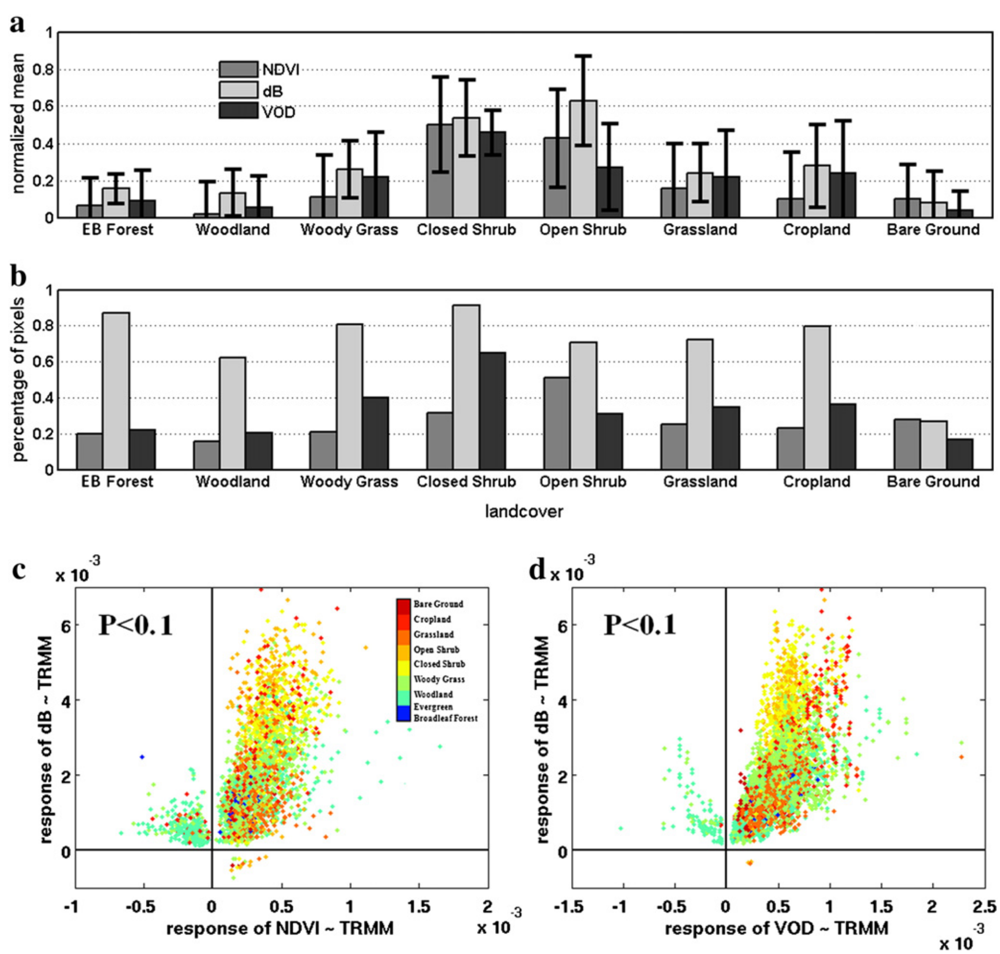

Fig. 5. (a) Normalized inter-annual sensitivity of NDVI/dB/VOD to TRMM precipitation. The normalization is done such that the maximum and minimum values correspond to 1 and 0 for each type of the RS datasets. The error bars give the standard deviation of the normalized sensitivity. 'EB Forest' refers to evergreen broadleaf forest. (b) Percentage of pixels satisfying significance level ($P<0.1$) in linear regression between annual growing-season RS fields and precipitation, for each land cover type. (c) Scatterplot of the inter-annual sensitivity of NDVI–TRMM and dB–TRMM, pixels with significant correlations ($P<0.1$) in both cases are shown here. (d) Scatterplot of the inter-annual sensitivity of VOD–TRMM and dB–TRMM. The color shadings correspond to land cover types.

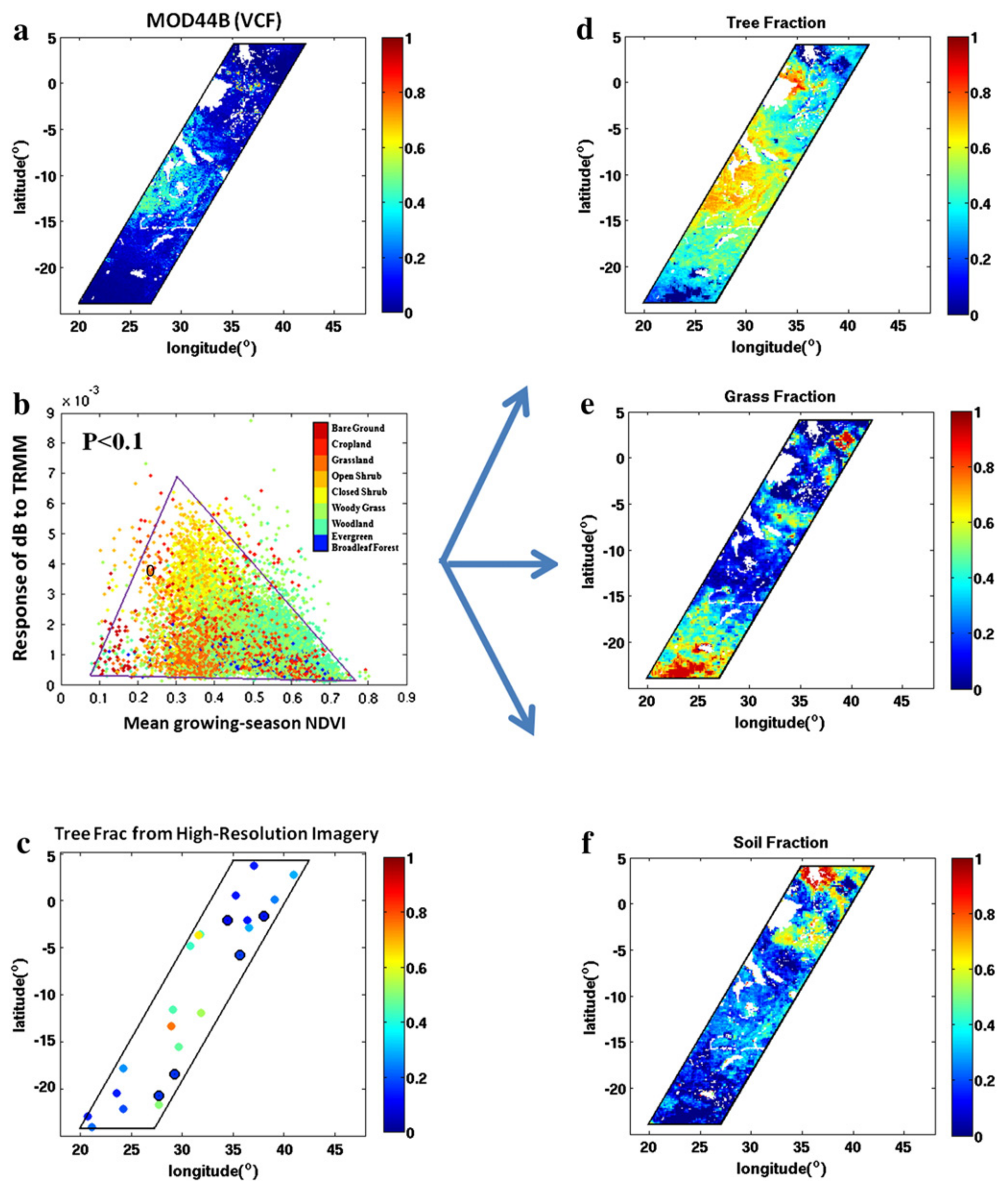

Fig. 6. (a) Tree fraction from MOD44B VCF product averaged from 2000 to 2005. (b) The 'Mean-Sensitivity Space' combining mean NDVI as x-axis, and inter-annual sensitivity of dB to precipitation as y-axis, with the optimal fitted triangle. Newly derived fractional covers for tree(d), grass(e) and bare soil(f) are presented. (c) Tree fraction from the classification results of the high-resolution imagery, cropland-mixed points are identified with black circles, and other points are natural vegetation.

important for justifying our multi-sensor approach and its future application. We propose the following simplified physical interpretations for the three RS datasets based on our results and the literature review:

$$\mathrm{NDVI} = F_1\left(P, f_t, f_g\right) F_4(\mathrm{cloudiness}, P) + \varepsilon_1 \quad (6)$$

$$\mathrm{dB} = F_2\left(P, f_t, f_g\right) + F_5(P, f_s) + \varepsilon_2 \quad (7)$$

$$\mathrm{VOD} = F_3\left(P, f_t, f_g\right) + F_6(P, f_s) + \varepsilon_3 \quad (8)$$

where P refers to precipitation; F_1 , F_2 and F_3 are vegetation response functions of NDVI, dB and VOD, respectively; F_4 describes the nonlinear cloudiness effects on Vis–NIR-based NDVI (i.e. more clouds lower the value of NDVI, and lead to smaller F4, and vice versa); F_5 and F_6 describe the soil moisture contribution for microwave sensors; ε_1, ε_2 and ε_3 are other impact factors which vary little inter-annually. NDVI signal also has some contribution from background soil, and this term has been included in ε_1 as it is much less important than F_4 for NDVI, especially in the tropics. The physical interpretations of F1, F2 and F3 are proposed as follows:

F_1: describes the landscape-integrated canopy-level leaf chlorophyll and photosynthetic intensity (Sellers et al., 1992).
F_2: describes the landscape-integrated vegetation canopy biomass (depending on wavelength for penetrating ability) and top-canopy water content (including interception and leaf water content) (Jarlan et al., 2002; Wagner et al., 1999a). In this case, Ku-band dB only detects the top-canopy information due to its relatively small wavelength which is unable to penetrate the whole canopy.
F_3: describes the landscape-integrated total water column through the whole canopy (Jones et al., 2010).

We assume the overall signals are a weighted summation of different plant-functional-types (PFTs) within each pixel, and interactions among

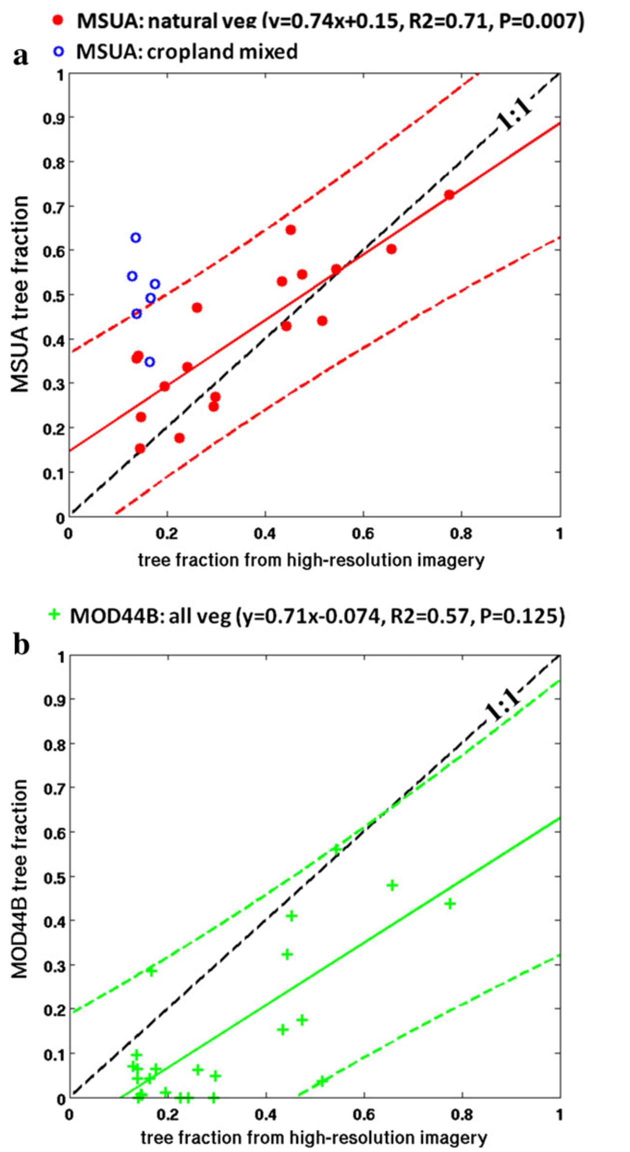

Fig. 7. (a) Comparison of the MSUA-derived tree fractional covers with the classification results from high-resolution imagery. Red dots refer to the tree fractional covers of natural vegetation, with linear fitting in red line and 95% confidence interval in red dashed line. Blue dots refer to the validation points partially containing cropland, and their tree fractions are overestimated in the MSUA. (b) Comparison of the mean tree fractional covers (from 2000 to 2005) from the MOD44B VCF with the classification results from high-resolution imagery, with linear fitting in green line and 95% confidence interval in green dashed line.

different PFTs and between PFTs and bare soil are neglected in the MSUA. The latter assumption has its limitation since the off-nadir view of the medium/coarse-resolution sensors (e.g. AVHRR and QuikSCAT) observes a three-dimensional landscape rather than two-dimension. Fortunately this limitation is moderated in the MSUA approach since the MSUA uses the 10-year mean vegetation states and the regressed sensitivity of vegetation to precipitation, such that the result is much less sensitive to short-term variabilities/errors in the RS dataset (Scanlon et al., 2002).

The proposed physical interpretations can account for the differences in the observed seasonality in Hovmöller Diagrams (Fig. 8), which is the zonal average of half-monthly mean of each dataset. Leaf chlorophyll and photosynthetic intensity carried by NDVI do not exhibit strong signals in the early stage of rainy season, due to the small fraction of vegetation. As the rainy season progresses, vegetation fraction expands, and photosynthetic rate of individual plant also increases, both of which lead to an increase in NDVI with a certain lag time after the precipitation. The various lags between NDVI and precipitation show the difference in response time for different PFTs (i.e. grass and tree) to precipitation inputs. dB responds quickly to precipitation, which results from the early green-up in top-canopy leaves, leaf water interception and instantaneous response of soil moisture. In the early rainy season, soil moisture in bare soil accounts for the major variability in the dB signal because of the low biomass, small vegetation fraction and large bare soil fraction, all of which lead to a shorter lag of dB to precipitation compared with the lag of NDVI to precipitation. In the late rainy season, biomass dominates the dB signal with various time lags after precipitation, which also reflects the difference in response to precipitation for different land cover types. VOD's seasonality has larger lags compared to NDVI and dB for woodland; the difference is less obvious for grassland/shrubland; and there is almost no difference in the most northern part, where bare ground dominates. The radiative surface emission model defines VOD as the attenuation medium of brightness temperature signal (T_b) from the underlying soil moisture passing through the whole canopy (Jones et al., 2010, 2011). The lagged response of VOD is consistent with the understanding that water content within a tree can usually accumulate till the end of rainy season, but not necessarily for biomass (Jones et al., 2010).

The proposed physical interpretations also explain the differences of inter-annual sensitivity to precipitation in the three RS datasets (i.e. $\frac{\mathrm{d(NDVI)}}{dP}$, $\frac{\mathrm{d(dB)}}{dP}$ and $\frac{\mathrm{d(VOD)}}{dP}$), which are expressed in the following way:

$$\frac{\mathrm{d(NDVI)}}{dP} = \frac{d(F_1)}{dP}F_4 + \frac{d(F_4)}{dP}F_1 \tag{9}$$

$$\frac{d(dB)}{dP} = \frac{d(F_2)}{dP} + \frac{d(F_5)}{dP} \tag{10}$$

$$\frac{d(VOD)}{dP} = \frac{d(F_3)}{dP} + \frac{d(F_6)}{dP} \tag{11}$$

The left-hand side of the equations are the regressed sensitivity from the data, but the terms $\frac{d(F_1)}{dP}$, $\frac{d(F_2)}{dP}$, $\frac{d(F_3)}{dP}$ in the right-hand side of the equations represent the actual vegetation sensitivity to precipitation, confounded by other terms which can be treated as noise in this study. The noise terms are mainly caused by either cloud covers or background soil moisture. Since all the datasets contain vegetation signals and noise, the signal-to-noise ratio (SNR) of each dataset becomes the primary concern. In Eq. (9), the term $\frac{\mathrm{d}(F_4)}{dP}$ could be negative during rainy seasons when increased precipitation associates with more clouds, which suppress NDVI signals (Tang & Oki, 2007; also see Section 4.2 for detailed discussion). The product of this negative term and positive $\frac{\mathrm{d(F1)}}{dP}$ may result in a large negative term, which may result in a negative $\frac{\mathrm{d(NDVI)}}{dP}$.

Vegetation sensitivity of dB (Eq. 10) is affected by soil moisture term $\frac{d(F_5)}{dP}$. The Hovmöller Diagrams (Fig. 8) show that soil moisture plays some role in explaining dB's intra-annual variation, especially in the early phase of rainy seasons when vegetation fraction is small. This means dB may not be a good indicator for assessing vegetation intra-annual variability. But dB's inter-annual sensitivity of bare soil to precipitation is very low (Section 3.2 and Fig. 5), i.e. soil moisture for a pure bare soil pixel has little sensitivity to precipitation at the inter-annual level. This is because the Ku-band dB used here can only detect the soil moisture from less than 1 cm depth (Frison et al., 1998; Mladenova et al., 2009; Scipal et al., 2002; Wagneret al., 1999b). The moisture in the shallow top soil layer that Ku-band dB is sensitive to saturates rapidly, which makes dB have little inter-annual sensitivity to precipitation on bare soil. Since the overall inter-annual sensitivity of a pixel is a weighted average from both vegetation and bare soil, the soil moisture contribution to the overall pixel sensitivity is relatively small compared to that from vegetation, especially in the regions where bare soil fraction is low, such as in woodland.

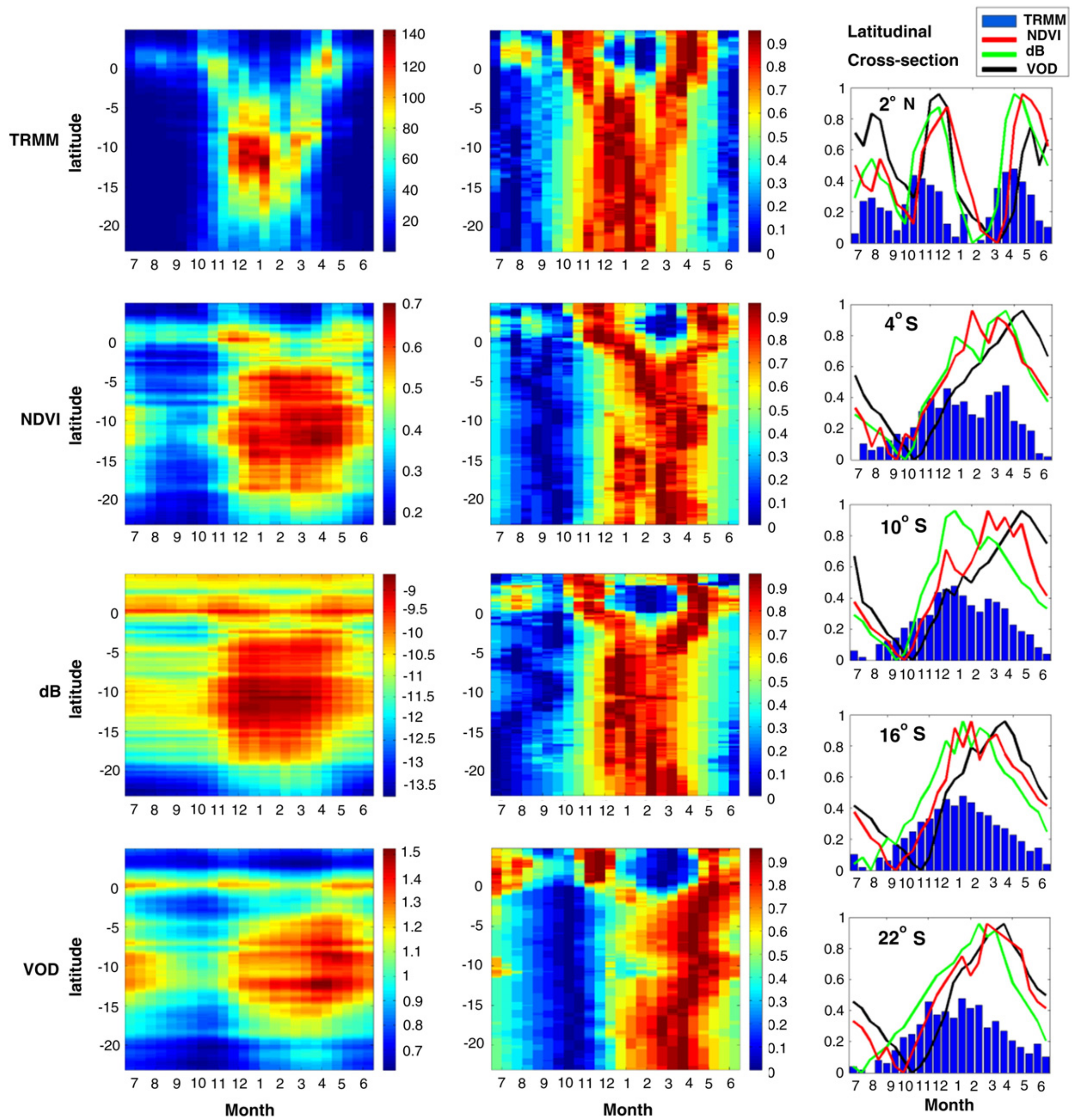

Fig. 8. The Hovmöller Diagram (zonal averaging for the same period) for TRMM, NDVI, dB and VOD. (Left column) the Hovmöller Diagram of raw value; (middle column) the Hovmöller Diagram with ranked values for the same latitude, with 0 and 1 representing minimum and maximum at a specific latitude. (Right column) Selected latitudinal cross-sections in Hovmöller Diagram of ranked values for different datasets, for better illustration of time series.

4.2. NDVI sensitivity to precipitation

We attribute the negative sensitivity of NDVI to precipitation to the degraded signal-to-noise ratio (SNR) due to the cloud effect, which is a common problem for Vis–NIR-based sensors. Alternatively, excessive precipitation is usually accompanied by increased cloud covers in tropical regions, leading to decreased photosynthetic active radiation (PAR), thus limiting ecosystem productivity. The same argument underpins an unresolved debate about the Amazonian green-up during the 2005 drought, which was primarily found from another Vis–NIR-based vegetation index, the Enhanced Vegetation Index (EVI) (Asner & Alencar, 2010; Ollinger, 2010; Saleska et al., 2007; Samanta et al., 2010).

We argue that the inter-annual sensitivity of NDVI to precipitation resulted from the interplay among precipitation, cloud and vegetation: (1) vegetation sensitivity to precipitation decreases with precipitation (Fig. 9a); (2) cloudiness increases with precipitation (Fig. 9b). These two patterns lead to the variable NDVI sensitivity in different precipitation ranges (Fig. 9c). When precipitation is below 650 mm/yr, vegetation sensitivity is high, while cloudiness impact is minimal, thus NDVI has a high SNR (corresponding to high coefficient of variation, CV). For the precipitation range from 650 mm/yr to 1200 mm/yr, vegetation sensitivity decreases, and cloud effect becomes pronounced and obscures the NDVI dynamics (decreased and flattened CV). Most negative NDVI sensitivity to precipitation appears in this precipitation range, because the low SNR of NDVI contains large uncertainties. When precipitation is above 1200 mm/yr, vegetation becomes insensitive to precipitation. dB's superiority over NDVI for assessing vegetation sensitivity mostly arises from dB's high SNR across all precipitation ranges, due to the ability of microwave sensors to penetrate cloud.

4.3. Uncertainties and limitations of multi-sensor MSUA approach

1) Though mean vegetation states is additive within a landscape for different PFTs, whether the sensitivity to precipitation is additive

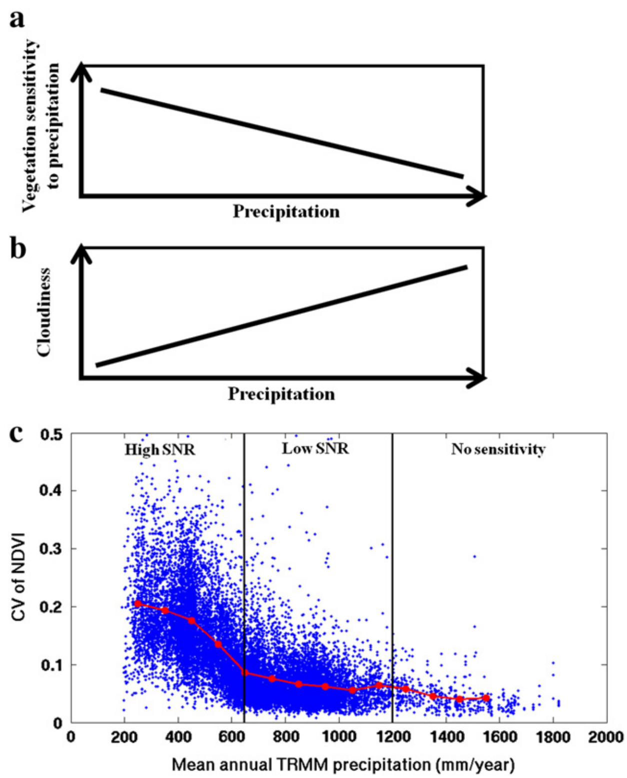

Fig. 9. (a) Conceptual diagram of vegetation sensitivity to precipitation as a function of mean annual precipitation (MAP). (b) Conceptual diagram of cloudiness as a function of MAP. (c) Coefficient of variation (CV) of mean growing-season NDVI for all the pixels as a function of MAP from TRMM, with the red dots refer to the mean CV values for each 100 mm/yr bin.

(or linearly) over the whole range of precipitation deserves more investigation.

2) The regressed sensitivity of vegetation to precipitation assumes little land cover changes happen during the study period, which makes the MSUA more valid for long-term fractional retrieval rather than a temporally dynamic fraction extraction.
3) The MSUA is more suitable for natural vegetation rather than regions with high human impacts (e.g. irrigated cropland), as shown in the validation section. The LAI of cropland usually ranges widely between grassland and woodland values. For highly-irrigated cropland, it would have little sensitivity to precipitation; for dry-land and rain-fed cropland, its response to precipitation would behave more like a grassland. Both cases are widely available in the Africa continent. Thus it is recommended that when applying the MSUA to larger areas, highly human-impacted regions should be excluded.

4.4. Ecohydrological implications from the derived vegetation fraction

Our results demonstrate the control of precipitation on the vegetation fractions. Fig. 10 shows that tree fraction reaches the plateau when precipitation is around 750 mm/yr; below that threshold value, tree fraction is controlled by MAP; and above that value, tree fraction is not responsive to MAP, which agrees with the prior field-data-based work (Sankaran et al., 2005). Grass cover peaks around 450 mm/yr; and below this value, it is controlled by MAP; above this value, it may be suppressed by tree fraction.

Another interesting pattern is revealed from the trajectory of latitudinally averaged fractional covers (only natural vegetation, excluding cropland-mixed pixels) and mean annual precipitation (MAP) over the transect (Fig. 11). Tree fraction follows the trajectory of MAP in general, and show peaks in the central portion of the transect. Both grass and bare soil fractions are suppressed by tree fraction in the central portion, but show opposite patterns in the northern and southern portion, both of which have low precipitation. Grass dominates the southern portion, while the northern portion has more bare soil, possibly resulted from the land degradation or geological factors.

5. Conclusion

We derived a new vegetation fractional cover product (including tree, grass and bare soil) along a large tropical savanna transect, that combines the advantages of Vis–NIR and microwave sensors, using an existing frame-work MSUA. Our product agrees with the tree fraction derived from high-resolution images for natural vegetation, but not necessarily for highly human-managed areas (e.g. irrigated cropland). Because our underlying datasets are global in nature, our approach has the potential to be applied at continental and global scales for natural vegetation.

In order to effectively implement the MSUA, we assessed the ability of three independent RS datasets for characterizing two key variables: mean vegetation states and vegetation inter-annual sensitivity to precipitation. We find NDVI and VOD have a reasonably high correlation in mean pixel values, and both are representative for different land cover types; while dB signal shows abnormally high value as more bare soil fraction present in the pixel. For inter-annual sensitivity to precipitation, microwave-based sensors, especially dB, largely overcome the cloudiness

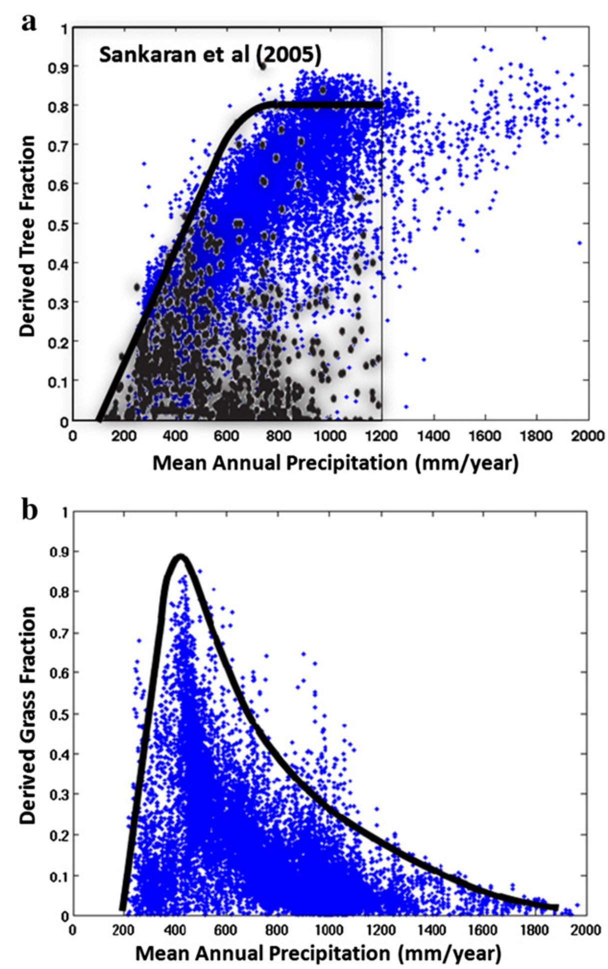

Fig. 10. (a) Derived tree fraction as a function of mean annual precipitation. Sankaran et al. (2005) tree fraction from field data is plotted in black above our derived results, showing the consistency in trend. (b) Derived grass fraction as a function of mean annual precipitation. Grass fraction peaks when mean annual precipitation (MAP) is around 450 mm; below this threshold, grass fraction is controlled by the MAP; above this threshold, grass fraction may be suppressed by increased tree fraction.

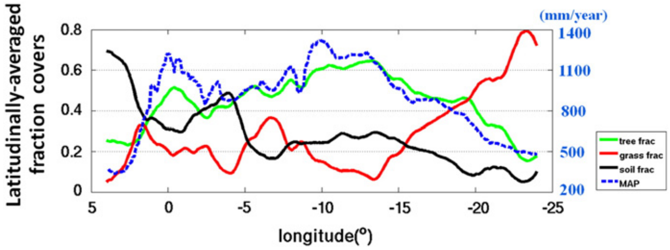

Fig. 11. Latitudinally averaged fractional covers (only natural vegetation, excluding cropland-mixed pixels) and mean annual precipitation (MAP) over the transect. Tree fraction follows the trajectory of MAP in general, and show peaks in the central portion of the transect. Both grass and bare soil fractions are suppressed by tree fraction in the central portion, but show opposite patterns in the northern and southern portion, both of which have low precipitation. Grass dominates the southern portion, while there is more bare soil in the northern portion. This result is consistent with the land cover pattern in Fig. 1.

problem found in NDVI, therefore can characterize more robust vegetation responses to precipitation. Our analysis provides insight to the interpretations of vegetation inter-annual variability of the different RS datasets, and identifies the possible source of uncertainties arisen from cloudiness and background soil moisture. This research will benefit the further RS application in ecosystem monitoring.

Acknowledgment

We thank Shi Li for his technical support of 'Simulated Annealing' algorithm. We are also grateful for the useful comments from the editor Scott Goetz and three anonymous reviewers, as well as from our colleagues: Haibin Li, Lixin Wang and Alok Sahoo. Justin Sheffield, Lucas Jones, Ronny Schroeder, Kyle C. McDonald, and John Kimball gave us constructive suggestions on the research. K.G. and E.F.W are supported by NASA via the grant NNX08AL59G. K.K.C. is supported by NSF via the grants BCS-1026334 and EAR-847368.

Appendix A. Supplementary data

Supplementary data to this article can be found online at http://dx.doi.org/10.1016/j.rse.2012.06.005.

References

Asner, G. P., & Alencar, A. (2010). Drought impacts on the Amazon forest: The remote sensing perspective. *New Phytologist*, *187*, 569–578.
Avissar, R., & Verstraete, M. M. (1990). The representation of continental surface processes in atmospheric models. *Reviews of Geophysics*, *28*, 35–52.
Caylor, K. K., DOdorico, P., & Rodriguez-Iturbe, I. (2006). On the ecohydrology of structurally heterogeneous semiarid landscapes. *Water Resources Research*, *42*, W07424.
Chopping, M., Nolin, A., Moisen, G. G., Martonchik, J. V., & Bull, M. (2009). Forest canopy height from the Multiangle Imaging SpectroRadiometer (MISR) assessed with high resolution discrete return lidar. *Remote Sensing of Environment*, *113*, 2172–2185.
Chopping, M. J., Rango, A., & Ritchie, J. C. (2002). Improved semi-arid community type differentiation with the NOAA AVHRR via exploitation of the directional signal. *IEEE Transactions on Geoscience and Remote Sensing*, *40* (5), 1132.
Chopping, M., Su, L., Rango, A., Martonchik, J. V., Peters, D. P., & Laliberte, A. (2008). Remote sensing of woody shrub cover in desert grasslands using MISR with a geometric-optical canopy reflectance model. *Remote Sensing of Environment*, *112* (1), 19–34.
DeFries, R. S., Townshend, J. R. G., & Hansen, M. C. (1999). Continuous fields of vegetation characteristics at the global scale at 1-km resolution. *Journal of Geophysical Research*, *104* (D14), 16,911–16,923.
Early, D. S., & Long, D. G. (2001). Image reconstruction and enhanced resolution imaging from irregular samples. *IEEE Transactions on Geoscience and Remote Sensing*, *39* (2), 291–302.
Ehleringer, J. R., & Monson, R. K. (1993). Evolutionary and ecological aspects of photosynthetic pathway variation. *Annual Review of Ecology and Systematics*, *24*, 411–439.
Friedl, M., McIver, D., Hodges, J., Zhang, X., Muchoney, D., Strahler, A., et al. (2002). Global land cover mapping from MODIS: Algorithms and early results. *Remote Sensing of Environment*, *83*, 287–302.
Frison, P. L., & Mougin, E. (1996). Monitoring global vegetation dynamics with ERS-1 wind scatterometer data. *International Journal of Remote Sensing*, *17* (16), 3201–3218.
Frison, P. L., Mougin, E., & Hiernaux, P. (1998). Observations and interpretation of seasonal ERS-1 wind scatterometer data over Northern Sahel (Mali). *Remote Sensing of Environment*, *63*, 233–242.
Frolking, S., Fahnestock, M., Milliman, T., McDonald, K., & Kimball, J. (2005). Interannual variability in North American grassland biomass/productivity detected by SeaWinds scatterometer backscatter. *Geophysical Research Letters*, *32*, L21409.
Frolking, S., Milliman, T., McDonald, K., Kimball, J., Zhao, M., & Fahne- stock, M. (2006). Evaluation of the SeaWinds scatterometer for regional monitoring of vegetation phenology. *Journal of Geophysical Research*, *111*, D17302.
Glenn, E. P., Huete, A. R., Nagler, P. L., & Nelson, S. G. (2008). Relationship between remotely-sensed vegetation indices, canopy attributes and plant physiological processes: What vegetation indices can and cannot tell us about the landscape. *Sensors*, *8*, 2136–2160.
Good, S. P., & Caylor, K. K. (2011). Climatological determinants of woody cover in Africa. *Proceedings of the National Academy of Sciences of the United States of America*, *108* (12), 4902–4907.
Grace, J. (2004). Understanding and managing the global carbon cycle. *Journal of Ecology*, *92* (2), 189–202.
Gutman, G., & Ignatov, A. (1998). The derivation of the green vegetation fraction from NOAA/AVHRR data for use in numerical weather prediction models. *International Journal of Remote Sensing*, *19* (8), 1533–1543.
Hansen, M. C., DeFries, R. S., Townshend, J. R. G., Carroll, M., Dimiceli, C., & Sohlberg, R. A. (2003). Global percent tree cover at a spatial resolution of 500 meters: First results of the MODIS vegetation continuous fields algorithm. *Earth Interactions*, *7*, 1–10.
Hardin, P. J., & Jackson, M. W. (2003). Investigating SeaWinds terrestrial backscatter: Equatorial savannas of South America. *Photogrammetric Engineering and Remote Sensing*, *69* (11), 1243–1254.
Heidinger, A. K., Anne, V. R., & Dean, C. (2002). Using MODIS to estimate cloud contamination of the AVHRR data record. *Journal of Atmospheric and Oceanic Technology*, *19* (5), 586.
Hirota, M., Holmgren, M., Nes, E. H. V., & Scheffer, M. (2011). Global resilience of tropical forest and savanna to critical transitions. *Science*, *334*, 232–235.
Holben, B. (1986). Characteristics of maximum-value composite images from temporal AVHRR data. *International Journal of Remote Sensing*, *7* (11), 1417–1434.
Huete, A., Liu, H., & van Leeuwen, W. (1997). The use of vegetation indices in forested regions: issues of linearity and saturation. Geoscience and Re-mote Sensing, 1997. *IGARSS '97. Remote Sensing—A Scientific Vision for Sustainable Development, 1997 IEEE International*, *4*. (pp. 1966–1968).
Huffman, G. J., Bolvin, D. T., Nelkin, E. J., Wolff, D. B., Adler, R. F., Bow- man, K. P., et al. (2007). The TRMM Multisatellite Precipitation Analysis (TMPA): Quasi-global, multiyear, combined-sensor precipitation estimates at fine scales. *Journal of Hydrometeorology*, *8*, 3855.
Jarlan, L., Mougin, E., Frison, P., Mazzeg, P., & Hiernaux, P. (2002). Analysis of ERS wind scatterometer time series over Sahel (Mali). *Remote Sensing of Environment*, *81*, 404–415.
Jones, L. A., Ferguson, C. R., Kimball, J. S., Zhang, K., Chan, S. K., McDon- ald, K. C., et al. (2010). Satellite microwave remote sensing of daily land surface air temperature minima and maxima from AMSR-E. *IEEE Journal of Selected Topics in Applied Earth Observations and Remote Sensing*, *3* (1), 111–123.
Jones, M. O., Jones, L. A., Kimball, J. S., & McDonald, K. C. (2011). Satellite passive microwave remote sensing for monitoring global land surface phenology. *Remote Sensing of Environment*, *115* (4), 1102–1114.
Jones, L. A., Kimball, J. S., Podest, E., McDonald, K. C., Chan, S. K., & Njoku, E. G. (2009). A method for deriving land surface moisture, vegetation optical depth, and open water fraction from AMSR-E. *Proc. IEEE Int. Geosci. Rem. Sens. Symp. (IGARSS 09), Cape Town, South Africa*.
K´efi, S., Rietkerk, M., Alados, C. L., Pueyo, Y., Papanastasis, V. P., ElAich, A., et al. (2007). Spatial vegetation patterns and imminent desertification in Mediterranean arid ecosystems. *Nature*, *449* (13), 213–217.
Laarhoven, P. J. M., van Laarhoven, P. J. M., & Aarts, E. H. L. (1988). *Simulated annealing: Theory and applications.* : Kluwer Academic Publisher.
Long, D. G., Hardin, P. J., & Whiting, P. T. (1993). Resolution enhancement of spaceborne scatterometer data. *IEEE Transactions on Geoscience and Remote Sensing*, *31* (3), 700–715.
Magagi, R., & Kerr, Y. (1997). Characterization of surface parameters over arid and semi-arid areas by use of ERS-1 windscatterometer. *Remote Sensing Reviews*, *15*, 133–155.
Mayaux, P., Holmgren, P., Achard, F., Eva, H., Stibig, H. -J., & Anne (2005). Tropical forest cover change in the 1990s and options for future monitoring. *Philosophical Transactions of the Royal Society of London. Series B, Biological sciences*, *360*, 373384.
McDonald, K. F. U. (1993). Radiative transfer modeling of discontinuous tree canopies at microwave frequencies. *International Journal of Remote Sensing*, *14* (11), 2097–2128.
Miles, L., Newton, A. C., DeFries, R. S., Ravilious, C., May, I., Blyth, S., et al. (2006). A global overview of the conservation status of tropical dry forests. *Journal of Biogeography*, *33*, 491505.
Mladenova, I., Lakshmi, V., Walker, J. P., Long, D. G., & Jeu, R. D. (2009). An assessment of QuikSCAT Ku-Band Scatterometer data for soil moisture sensitivity. *IEEE Geoscience and Remote Sensing Letters*, *6* (4), 640–643.
Naderi, F. M., Freilich, M. H., & Long, D. G. (1991). Spaceborne radar measurement of wind velocity over the ocean—An overview of the NSCAT scatterometer system. *Proceedings of the IEEE*, *79* (6), 850–866.
Njoku, E. G., & Chan, S. K. (2006). Vegetation and surface roughness effects on AMSR-E land observations. *Remote Sensing of Environment*, *100*, 190–199.
Okin, G. S. (2007). Relative spectral mixture analysis a multitemporal index of total vegetation cover. *Remote Sensing of Environment*, *106*, 467479.
Ollinger, S. (March 15). NASA terrestrial ecosystems research. *NASA Terrestrial Ecology Program Meeting, La Jolla, California*.

Owe, M., de Jeu, R., & Walker, J. (2001). A methodology for surface soil moisture and vegetation optical depth retrieval using the microwave polarization difference index. *IEEE Transactions on Geoscience and Remote Sensing*, *39* (8), 1643–1645.

Randerson, J. T., Thompson, M. V., Conway, T. J., Fung, I. Y., & Field, C. B. (1997). The contribution of terrestrial sources and sinks to trends in the seasonal cycle of atmospheric carbon dioxide. *Global Biogeochemical Cycles*, *11* (4), 535–560.

Rodriguez-Iturbe, I., & Porporato, A. (2004). *Ecohydrology of water-controlled ecosystem: Soil moisture and plant dynamics.* New York: Cambridge University Press.

Saleska, S. R., Didan, K., Huete, A. R., & da Rocha, H. R. (2007). Amazon forests green-up during 2005 drought. *Science*, *318*, 612.

Samanta, A., Ganguly, S., Hashimoto, H., Devadiga, S., Vermote, E., Knyazikhin, Y., et al. (2010). Amazon forests did not green-up during the 2005 drought. *Geophysical Research Letters*, *37*, L05401.

Sankaran, M., Hanan, N. P., Scholes, R. J., Ratnam, J., Augustine, D. J., Cade, B. S., et al. (2005). Determinants of woody cover in African savannas. *Nature*, *438* (8), 846–849.

Scanlon, T. M., & Albertson, J. D. (2003). Inferred controls on tree/grass composition in a savanna ecosystem: Combining 16-year normalized difference vegetation index data with a dynamic soil moisture model. *Water Resources Research*, *39* (8), 1224.

Scanlon, T. M., Albertson, J. D., Caylor, K. K., & Williams, C. A. (2002). Determining land surface fractional cover from NDVI and rainfall time series for a savanna ecosystem. *Remote Sensing of Environment*, *82*, 376–388.

Scholes, R. J., & Archer, S. R. (1997). Tree–grass interactions in savannas. *Annual Review of Ecology and Systematics*, *28*, 517–544.

Scholes, R., Dowty, P., Caylor, K., Parsons, D., Frost, P., & Shugart, H. (2002). Trends in savanna structure and composition along an aridity gradient in the Kalahari. *Journal of Vegetation Science*, *13*, 419–428.

Scholes, R. J., & Walker, B. H. (1993). *An African savanna: Synthesis of the Nylsvley Study.* New York: Cambridge University Press.

Scipal, K., Wagner, W., & Kidd, R. (2002). Comparison of Ku- and C-band backscatter time series over land. *Geoscience and Remote Sensing Sympo- sium, 2002. IGARSS 02, 2428 June, Toronto, Canada (IEEE International)*, *3*. (pp. 1343–1345).

Sellers, P. J., Berry, J. A., Collatz, G. J., Field, C. B., & Hall, E. G. (1992). Canopy reflectance, photosynthesis, and transpiration. III. A reanalysis using improved leaf models and a new canopy integration scheme. *Remote Sensing of Environment*, *42*, 187–216.

Shi, J., Jackson, T., Tao, J., Du, J., Bindlish, R., Lu, L., et al. (2008). Microwave vegetation indices for short vegetation covers from satellite passive microwave sensor AMSR-E. *Remote Sensing of Environment*, *112*, 4285–4300.

Tang, Q., & Oki, T. (2007). Daily NDVI relationship to cloud cover. *Journal of Applied Meteorology and Climatology*, *46*, 377–387.

Tanre, D., Holben, B. N., & Kaufman, Y. J. (1992). Atmospheric correction algorithm for NOAA-AVHRR products: Theory and application. *IEEE Transactions on Geoscience and Remote Sensing*, *30*(2), 231–248.

Tucker, C. J., Pinzon, J. E., Brown, M. E., Slayback, D. A., Paka, E. W., Mahoney, R., et al. (2005). An extended AVHRR 8-km NDVI dataset compatible with MODIS and SPOT vegetation NDVI data. *International Journal of Remote Sensing*, *26* (20), 4485–4498.

Ulaby, F., Moore, R., & Fung, A. (1982). *Microwave remote sensing: Active and passive, Volume 2: Radar remote sensing and surface scattering and emission theory.* Reading, MA: Addison-Wesley.

Ulaby, F., Sarabandi, K., McDonald, K., Whitt, M., & Dobson, M. C. (1990). Michigan microwave canopy scattering model. *International Journal of Remote Sensing*, *11* (7), 1223–1253.

Viovy, N., Arino, O., & Belward, A. S. (1992). The best index slope extraction (BISE): A method for reducing noise in NDVI time-series. *International Journal of Remote Sensing*, *13* (8), 1585–1590.

Wagner, W., Lemoine, G., Borgeaud, M., & Rott, H. (1999a). A study of vegetation cover effects on ERS scatterometer data. *IEEE Transactions on Geoscience and Remote Sensing*, *37* (2), 938–948.

Wagner, W., Lemoine, G., & Rott, H. (1999b). A method for estimating soil moisture from ERS Scatterometer and soil data. *Remote Sensing of Environment*, *70*, 191–207.

Zeng, X., Dickinson, R. E., Walker, A., Shaikh, M., Defries, R. S., & Qi, J. (2000). Derivation and evaluation of global 1-km fractional vegetation cover data for land modeling. *Journal of Applied Meteorology*, *39*, 826–839.

Zhao, M., Heinsch, F. A., Nemani, R. R., & Runninga, S. W. (2005). Improvements of the MODIS terrestrial gross and net primary production global data set. *Remote Sensing of Environment*, *95*, 164176.

Zine, S., Jarlan, L., Frisona, P. -L., Mougin, E., Hiernaux, P., & Rudant, J. -P. (2005). Land surface parameter monitoring with ERS scatterometer data over the Sahel: A comparison between agro-pastoral and pastoral areas. *Remote Sensing of Environment*, *96*, 438–452.